Second harmonic helicity and Faraday rotation in gated single-layer $1T'$ -WTe$_2$

Pankaj Bhalla and Habib Rostami

Nordita, KTH Royal Institute of Technology and Stockholm University, Hannes Alfvéns väg 12, 114 21 Stockholm, Sweden

A single layer of the $1T'$ phase of WTe$_2$ provides a rich platform for exotic physical properties such as the nonlinear Hall effect and high-temperature quantum spin Hall transport. Utilizing a continuum model and the diagrammatic method, we calculate the second harmonic conductivity of monolayer $1T'$-WTe$_2$ modulated by an external vertical electric field and electron doping. We obtain a finite helicity and Faraday rotation for the second harmonic signal in response to linearly polarized incident light in the presence of time-reversal symmetry. The second harmonic signal's helicity is highly controllable by altering the bias potential and serves as an optical indicator of the nonlinear Hall current. Our study motivates future experimental investigation of the helicity spectroscopy of two-dimensional materials.

I. INTRODUCTION

Two-dimensional (2D) materials such as transition metal dichalcogenides (TMDs), with the chemical formula MX_2, where M stands for the transition metal atom (W, Mo) and X is the chalcogen atom (Te, Se, or S), appear in different crystalline structures such as hexagonal ($2H$), tetragonal ($1T$), and distorted ($1T'$ and $1T_d$) structures [1–3]. Noncentrosymmetric TMDs exhibit unique physical properties such as circular dichroism, piezoelectricity, the nonlinear Hall effect, and second harmonic generation due to their distinct phases [4–15]. The distorted 2D WTe$_2$ has attracted a surge of interest due to diverse ground state phases such as quantum spin Hall, superconductivity, polar metals, and ferroelectricity [16–20].

The $1T$ phase of WTe$_2$ has a rhombohedral (ABC) stacking with one tungsten layer sandwiched between two tellurium layers and has D_{3d} point group [21]. However, the freestanding $1T$ system is unstable, and it undergoes a spontaneous lattice distortion to form a period-doubling distorted structure known as the $1T'$ phase with point group C_{2h} [22]. Note that the metal atoms in the $1T'$ phase rearrange in the zigzag chain. The $1T'$ phase possesses mirror plane symmetry $\mathcal{M}_x$ perpendicular to the x direction and twofold rotational symmetry C_{2x} and hence remains $\mathcal{I} = \mathcal{M}_x C_{2x}$ inversion symmetric [16,23–25]. Moreover, the monolayer $1T_d$ structure, with point group C_{1s} [26], breaks the twofold rotational symmetry because it has more distortion than the $1T'$ phase and preserves the mirror symmetry $\mathcal{M}_x$; hence, it breaks the inversion symmetry [26]. As a result of this inversion symmetry breaking, a

weak intrinsic in-plane displacement field emerges in the $1T_d$ structure, and the dispersion is spin polarized.

By applying an external vertical electric field in a dual-gated system of distorted ($1T'$ and $1T_d$) WTe$_2$, one can efficiently create a controllable displacement field [26] similar to the case of a biased bilayer graphene [27–30] [see Fig. 1(a)]. Upon the use of a strong external electric field, the field-induced band gap dominates the intrinsic one in the $1T_d$ phase. In the absence of the spin-orbit interaction and the vertical field, the low-energy dispersion of WTe$_2$ reveals
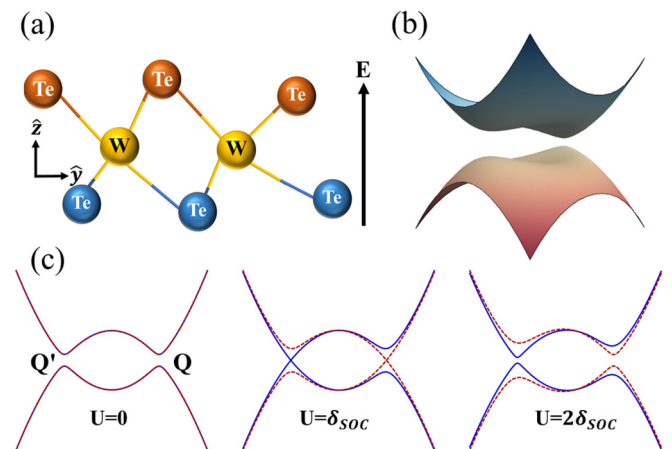

FIG. 1. (a) Lattice-distorted $1T'$ structure of WTe$_2$ in the presence of an external vertical electric field $\boldsymbol{E}$, where the top and bottom atomic layers are shown in different colors. (b) Energy dispersion of single-layer $1T'$-WTe$_2$ in the momentum space with the finite bias potential U. (c) Dispersion along the k_x direction at different bias potentials, $U = 0$, $U = \delta_{\text{SOC}}$, and $U = 2\delta_{\text{SOC}}$, where the blue solid curve shows the spin index $s = +1$ and the red dashed curve shows $s = -1$. Here $\mathbf{Q}' = -\mathbf{Q}$, and the spin-orbit coupling strength $\delta_{\text{SOC}} = v_x Q$, where v_x parametrizes the electron velocity along the x direction at large k_x. We have neglected the tilt in the schematic dispersion in order to highlight the topological features.

two topologically protected tilted Dirac cones in the neighborhood of the Γ point [31–33]. The spin-orbit-induced band inversion drives the system into a quantum spin Hall phase at a reasonably high temperature (100 K) [25,34–37]. The schematic view of the $1T'$-WTe$_2$ dispersion is shown in Fig. 1. The energy bands are degenerate at zero bias potential with a band gap due to the spin-orbit interaction. However, the band degeneracy breaks if the bias potential U is turned on. Interestingly, on U approaching the strength of the spin-orbit coupling δ_{SOC}, the spin-polarized band gap vanishes around one Dirac point. With more distortion ($U > \delta_{\text{SOC}}$), the bands remain nondegenerate, and the gap again opens up, as shown in Fig. 1(c).

Strong and diverse forms of nonlinear response in 2D materials are drawing attention for applications in all-optical modulators [38–43]. Especially, a strong nonlinear Hall response has been measured in single-layer and bilayer WTe$_2$ that can be described in terms of the Fermi surface average of the Berry curvature derivative, the so-called Berry curvature dipole [44–61]. The second harmonic generation (SHG) is utilized to measure the internal lattice distortion (strain) in 2D crystals [62]. The dynamical form of the nonlinear Hall effect manifests in the second harmonic transverse current in response to the linearly polarized light in noncentrosymmetric 2D materials such as biased single- and few-layer WTe$_2$ [58,63–67]. Interestingly, theoretical studies have provided the direct correspondence of high harmonic helicity (circular dichroism) and the topological nature of the electronic band structure [68,69]. For instance, it has been shown that the nonlinear helicity spectroscopy can sharply distinguish between trivial and topological phases of the Haldane model in the hexagonal 2D materials [70,71].

Despite extensive studies of all-optical amplitude modulation, the phase and polarization modulation of the second harmonic signal have not been systematically studied in TMD materials. Faraday rotation and dichroism effects can be employed to explore the polarization of second harmonic radiation. The Faraday effect is the rotation of the polarization plane of a linearly polarized light upon its propagation through a medium [72–80] which decomposes the linear polarized light into left- and right-handed circular components. In isotropic materials, the Faraday rotation emerges only after breaking the time-reversal symmetry. In such cases, the left- and right-handed components of the polarized light experience different refraction index and hence propagate with different phase velocities that lead to the rotation of a polarization plane (Faraday rotation) as well as finite ellipticity (helicity). The nonlinear Hall effect does not require time-reversal symmetry to be broken, and therefore, a finite helicity and Faraday rotation are expected for the SHG signal. To the best of our knowledge, the SHG signal's polarization in single-layer $1T'$-WTe$_2$ has not been explored microscopically.

This study aims to fill this gap by developing a microscopic continuum analysis of the polarization and amplitude modulations in single-layer $1T'$-WTe$_2$. We study the second harmonic response for the time-reversal symmetric and distorted $1T'$-WTe$_2$ in the presence of a vertical electric field. We first propose the theory for the nonlinear Faraday rotation angle and the second harmonic helicity in terms of the second-order optical conductivity. We explore the effects of bias

potential induced by the vertical electric field on the second harmonic susceptibility, Faraday rotation angle, and second harmonic helicity. We find that significantly large helicity can be achieved near the interband transitions. A linear light with frequency ω can be effectively converted to a circularly polarized light with frequency 2ω. The process is controllable by the interplay of the Fermi energy and the bias potential.

II. THEORETICAL METHOD

We consider a low-energy model in the 2D momentum space for the distorted $1T'$ phase of WTe$_2$, which is described as [26]

$$\hat{\mathcal{H}} = \{Ak^2\hat{I} + (\delta + Bk^2)\hat{\sigma}_z + v_y k_y \hat{\sigma}_y + U\hat{\sigma}_x\} \otimes \hat{s}_0 + v_x k_x \hat{\sigma}_x \otimes \hat{s}_y. \tag{1}$$

The spin-mixing term $U'\hat{\sigma}_y \otimes \hat{s}_x$ is neglected since, usually, we have $U \gg U'$ [26]. Notice that $\hat{s}_0$ is the identity matrix in the spin basis and $\hat{s}_{i=x,y}$ correspond to the spin Pauli matrices. The Pauli matrices $\hat{\sigma}_{i=x,y,z}$ and identity matrix $\hat{I}$ are in the orbital basis $\{\psi_+, \psi_-\} = \{p$ orbital of Te, d orbital of W$\}$, which is separated by the fundamental gap 2δ at the Γ point. Here U represents the coupling between the out-of-plane electric field and the orbitals, with the wave vector $\boldsymbol{k} = (k_x, k_y)$ having $k = |\boldsymbol{k}|$. The $\boldsymbol{k} \cdot \boldsymbol{p}$ parameters v_x, v_y, A, and B are obtained after fitting to realistic low-energy dispersion of $1T'$-WTe$_2$ [26,81]. In our analysis, we focus on the impact of bias potential U on the nonlinear response of the system.

Since $\hat{s}_y$ and $\hat{s}_0$ commute, using a unitary transformation, we obtain the Hamiltonian in a spin basis where $\hat{s}_y \rightarrow s = \pm$ is diagonal. Then, we calculate eigenvalues $\varepsilon_{\boldsymbol{k},s}^\lambda$, eigenvectors $|u_{\boldsymbol{k},s}^\lambda\rangle$, and then matrix elements $\langle u_{\boldsymbol{k},s}^{\lambda_1}|\hat{O}|u_{\boldsymbol{k},s}^{\lambda_2}\rangle$, in which $\hat{O}$ stands for the paramagnetic and diamagnetic current operators' elements, required for the response function evaluation. Corresponding to the Hamiltonian (1), the energy dispersion is given by

$$\varepsilon_{\boldsymbol{k},s}^\lambda = Ak^2 + \lambda\sqrt{(\delta + Bk^2)^2 + v_y^2 k_y^2 + (U + sv_x k_x)^2}, \tag{2}$$

and the eigenvectors are $|u_{\boldsymbol{k},s}^\lambda\rangle = 1/\sqrt{2}[\sqrt{1 \pm b_{k,s}}, \sqrt{1 \mp b_{k,s}}]$, where $b_{k,s} = (\delta + Bk^2)/E_{k,s}$, with $E_{k,s} = [(\delta + Bk^2)^2 + \hbar^2 v_y^2 k_y^2 + (U + sv_x k_x)^2]^{1/2}$, and $\lambda = + (-)$ for the conduction (valence) band. In addition to the time-reversal symmetry, this model also possesses the mirror symmetry along the $\hat{x}$ direction, which ensures the dispersion $\varepsilon(k_x, k_y) = \varepsilon(-k_x, k_y)$. In the absence of bias potential, $U = 0$, and for $\delta/B < 0$, the system has two gapless nodes (valleys) at $\tau\boldsymbol{Q} = (\tau\sqrt{|\delta/B|}, 0)$, with $\tau = \pm$ being the valley index. The schematic picture of the dispersion is shown in Fig. 1. The energy gap $2\Delta_\pm$ at the valley point $\tau\boldsymbol{Q}$ is given by $\Delta_\pm = U \pm v_x Q$ for each spin-valley index $\tau s = \pm$. Similar to the Kane-Mele model in graphene with spin-orbit coupling [82], $1T'$-WTe$_2$ is in the topological (i.e., quantum spin Hall) phase when $|v_x Q| > |U|$ and is trivial for $|v_x Q| < |U|$. The finite bias potential U breaks the inversion symmetry of the system, and it opens the gap around two points (Q points) in the Brillouin zone, as depicted in Fig. 1. However, the time-reversal symmetry of the system remains preserved. Further, this externally tunable bias potential is an artifact of the in-plane electrical polarization induced by an
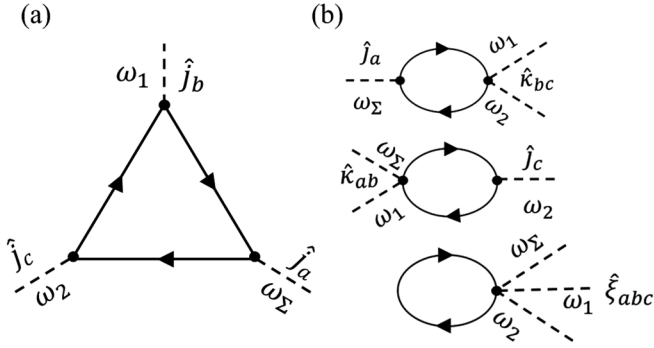
(a)   (b)

FIG. 2. Feynman diagrams for the (a) paramagnetic and (b) diamagnetic contributions to the second-order response. Here solid lines indicate the electron propagators, and dotted lines refer to external photons. The symbol ω_i represents the incoming and outgoing frequencies, $\omega_\Sigma = \omega_2 + \omega_2$, and $\hat{j}_a$, $\hat{\kappa}_{ab}$, and $\hat{\xi}_{abc}$ denote one-, two-, and three-photon current vertices, respectively.

external out-of-plane electric field due to the intrinsic lattice distortion, as displayed in Fig. 1(a) [26].

A. Nonlinear response of gated 1T'-WTe₂

Light-matter interaction is modeled via minimal coupling $\hbar \boldsymbol{k} \rightarrow \hbar \boldsymbol{k} + e\boldsymbol{A}(t)$, where $\boldsymbol{A}(t)$ is an external vector potential.

Due to the nonlinear dispersion of the Hamiltonian, both one- and two-photon couplings are present [83]. We begin with the phenomenological relation of the second-order current in the frequency domain in response to an external vector potential $\boldsymbol{A}(t)$, with the time-dependent and spatial homogeneous electric field $\boldsymbol{E}(t) = -\partial_t \boldsymbol{A}(t)$ [75],

$$J_a^{(2)}(\omega_\Sigma) = \sum_{\omega_1,\omega_2} \sum_{bc} \chi_{abc}^{(2)}(\omega_\Sigma; \omega_1, \omega_2) A_b(\omega_1) A_c(\omega_2)$$
$$\times \delta(\omega_\Sigma - \omega_1 - \omega_2). \tag{3}$$

Here we define $\boldsymbol{A}(\omega) = -i\boldsymbol{E}(\omega)/\omega$, and the δ function implies that $\omega_\Sigma = \omega_1 + \omega_2$. For the sake of convenience, we write the tensor quantity as $\chi_{abc}^{(2)}(\omega_1, \omega_2)$ in further calculations. The latter second-order response tensor includes two terms [83,84]:

$$\chi_{abc}^{(2)}(\omega_1, \omega_2) = \chi_{abc}^{(2),D}(\omega_1, \omega_2) + \chi_{abc}^{(2),P}(\omega_1, \omega_2), \tag{4}$$

where the terms $\chi_{abc}^{(2),D}$ and $\chi_{abc}^{(2),P}$ refer to the diamagnetic and paramagnetic contributions, respectively. The paramagnetic susceptibility, a three-point retarded correlation function of current operator components, is defined diagrammatically in Fig. 2(a).

Using the many-body diagrammatic perturbation theory, the second-order paramagnetic susceptibility after one performs the Matsubara frequency summation and then considers the analytic continuation $i\omega_n \rightarrow \omega + i\eta$, with $\eta \rightarrow 0^+$, can be expressed as [85–87]

$$\chi_{abc}^{(2),P}(\omega_1, \omega_2) = \sum_{\mathcal{P}} \sum_{\{\lambda_i\}} \sum_{\boldsymbol{k},s} \frac{j_a^{\lambda_1\lambda_2} j_b^{\lambda_2\lambda_3} j_c^{\lambda_3\lambda_1}}{\hbar\omega_\Sigma + \varepsilon_{\boldsymbol{k},s}^{\lambda_2} - \varepsilon_{\boldsymbol{k},s}^{\lambda_1} + i\eta} \left\{ \frac{f(\varepsilon_{\boldsymbol{k},s}^{\lambda_2}) - f(\varepsilon_{\boldsymbol{k},s}^{\lambda_3})}{\hbar\omega_1 + \varepsilon_{\boldsymbol{k},s}^{\lambda_2} - \varepsilon_{\boldsymbol{k},s}^{\lambda_3} + i\eta} - \frac{f(\varepsilon_{\boldsymbol{k},s}^{\lambda_3}) - f(\varepsilon_{\boldsymbol{k},s}^{\lambda_1})}{\hbar\omega_2 + \varepsilon_{\boldsymbol{k},s}^{\lambda_3} - \varepsilon_{\boldsymbol{k},s}^{\lambda_1} + i\eta} \right\}. \tag{5}$$

The one-photon coupling is the standard current vertex $\hat{j}_a = -(e/\hbar)\partial_{k_a}\hat{\mathcal{H}}$, which is also known as the paramagnetic current operator. Note that $\sum_{\mathcal{P}}$ stands for the intrinsic permutation symmetry $(b, \omega_1) \Longleftrightarrow (c, \omega_2)$. Here $f(\varepsilon_{\boldsymbol{k},s}^\lambda) = [1 + e^{\beta(\varepsilon_{\boldsymbol{k},s}^\lambda - \mu)}]^{-1}$ is the Fermi-Dirac distribution function, μ is the chemical potential, and $\beta = 1/k_B T$, where k_B is the Boltzmann constant and T is electron temperature. Similarly, the diamagnetic contribution to the second-order response according to Fig. 2(b) is given by

$$\chi_{abc}^{(2),D}(\omega_1, \omega_2) = \sum_{\mathcal{P}} \sum_{\{\lambda_i\}} \sum_{\boldsymbol{k},s} \left\{ \frac{j_a^{\lambda_1\lambda_2}\kappa_{bc}^{\lambda_2\lambda_1}[f(\varepsilon_{\boldsymbol{k},s}^{\lambda_2}) - f(\varepsilon_{\boldsymbol{k},s}^{\lambda_1})]}{\hbar\omega_1 + \varepsilon_{\boldsymbol{k},s}^{\lambda_1} - \varepsilon_{\boldsymbol{k},s}^{\lambda_2} + i\eta} + \frac{1}{2} \frac{(j_b^{\lambda_2\lambda_1}\kappa_{ac}^{\lambda_1\lambda_2} + j_c^{\lambda_2\lambda_1}\kappa_{ba}^{\lambda_1\lambda_2})[f(\varepsilon_{\boldsymbol{k},s}^{\lambda_2}) - f(\varepsilon_{\boldsymbol{k},s}^{\lambda_1})]}{\hbar\omega_\Sigma + \varepsilon_{\boldsymbol{k},s}^{\lambda_1} - \varepsilon_{\boldsymbol{k},s}^{\lambda_2} + i\eta} + \xi_{abc}^{\lambda_1\lambda_1} f(\varepsilon_{\boldsymbol{k},s}^{\lambda_1}) \right\}. \tag{6}$$

The two-photon and three-photon couplings are given by $\hat{\kappa}_{ab} = -(e/\hbar)^2 \partial_{k_a}\partial_{k_b}\hat{\mathcal{H}}$ and $\hat{\xi}_{abc} = -(1/2)(e/\hbar)^3 \partial_{k_a}\partial_{k_b}\partial_{k_c}\hat{\mathcal{H}}$, also termed the diamagnetic current operator in the context of superconductors. Considering the explicit form of the $\boldsymbol{k} \cdot \boldsymbol{p}$ Hamiltonian (1), the three-photon vertex is zero, and the only nonvanishing components of the two-photon vertex coupling are $\hat{\kappa}_{xx}$ and $\hat{\kappa}_{yy}$. However, in order to avoid the artifact in the low-energy model, we consider the three-photon coupling contribution by using a gauge invariance argument. Since the three-photon vertex diagram leads to a frequency-independent susceptibility, its contribution can be fixed by enforcing the gauge invariance. This is because the total susceptibility must vanish $\chi_{abc}^{(2)}(\omega_1 = 0, \omega_2 = 0) = 0$ for a homogeneous and time-independent gauge potential [83,86,88].

Due to the mirror symmetry $x \rightarrow -x$, the elements of second-order susceptibility $\chi_{abc}^{(2)}$ with an odd number of x

indices will vanish. The remaining nonvanishing components of the second harmonic susceptibility with an even number of x indices are $\chi_{yxx}^{(2)}$, $\chi_{xyx}^{(2)}$, $\chi_{xxy}^{(2)}$, and $\chi_{yyy}^{(2)}$, which we compute in the next section. Additionally, $\chi_{xxy}^{(2)} = \chi_{xyx}^{(2)}$ on interchanging the last two spatial indices by symmetry. Hence, one is left with three independent third-rank tensor components.

Using the total second-order susceptibility, one can obtain the second-order conductivity as follows:

$$\sigma_{abc}^{(2)}(\omega_1, \omega_2) = -\frac{\chi_{abc}^{(2)}(\omega_1, \omega_2)}{\omega_1\omega_2}. \tag{7}$$

Here we consider $\omega_1 = \omega_2 = \omega$ to compute second harmonic conductivities which will be further used below to obtain the polarization quantities such as the Faraday rotation and the helicity.

B. Second harmonic signal polarization

For the analytical derivation in the present study, we assume linearly polarized light with normal incidence and a generic polarization direction $\boldsymbol{E}(t) = \hat{\boldsymbol{\epsilon}}(\phi) E_0 e^{i(\mathbf{q} \cdot \mathbf{r} - \omega t)} + \text{c.c.}$ Here E_0 is the amplitude of the incident beam; $\hat{\boldsymbol{\epsilon}}(\phi) = \hat{x} \cos \phi + \hat{y} \sin \phi$ is the polarization direction, with ϕ being the polarization angle with the x axis, and the wave vector $\mathbf{q} = -\hat{\mathbf{z}} \omega / c$. At normal incidence, the second harmonic current (taking $\omega_1 = \omega_2 = \omega$) follows $\mathbf{J}^{(2)} = E_0^2 (a_x \hat{x} + a_y \hat{y})$, where the component of the response can be expressed as

$$a_j = \sigma^{(2)}_{jxx} (\cos \phi)^2 + \sigma^{(2)}_{jyy} (\sin \phi)^2 + \sigma^{(2)}_{jxy} \sin(2\phi). \quad (8)$$

Here we have used the symmetry relation $\sigma^{(2)}_{jxy} = \sigma^{(2)}_{jyx}$ in the last term. More specifically, the second harmonic current can be written in terms of the longitudinal (along the polarization direction) and transverse (normal to the polarization direction) components as $\mathbf{J}^{(2)} = J^{(2)}_L \hat{\boldsymbol{\epsilon}}(\phi) + J^{(2)}_T \hat{\mathbf{t}}(\phi)$, where the transverse direction $\hat{\mathbf{t}}(\phi) = \hat{\mathbf{z}} \times \hat{\boldsymbol{\epsilon}}(\phi)$. We define the longitudinal and transverse components of the nonlinear conductivity in the forms $\sigma^{(2)}_L = J^{(2)}_L / E_0^2 = a_x \cos \phi + a_y \sin \phi$ and $\sigma^{(2)}_T = J^{(2)}_T / E_0^2 = -a_x \sin \phi + a_y \cos \phi$. Here we consider $a_x = |a_x| e^{i\delta_x}$ and $a_y = |a_y| e^{i\delta_y}$, where δ_x (δ_y) refers to the phase associated with the $\hat{x}$ ($\hat{y}$) component of the response. In the circular basis representation ($\hat{l}, \hat{r}$), we can write $a_{r/l} \equiv a_x \pm i a_y$, where the $+ (-)$ sign stands for the right-handed (left-handed) circular counterpart. Using the circular decomposition along with the relation between the Stokes and polarization parameters [89–91], the Faraday rotation angle ψ is defined as

$$\tan(2\psi) = \frac{S_2}{S_1} = -\frac{\text{Im}[a_l^* a_r]}{\text{Re}[a_l^* a_r]}. \quad (9)$$

Here S_i denotes the Stokes parameters of the monochromatic light [89], such as $S_0 = |a_l|^2 + |a_r|^2$, $S_1 = 2\text{Re}[a_l^* a_r]$, $S_2 = -2\text{Im}[a_l^* a_r]$, and $S_3 = |a_l|^2 - |a_r|^2$. Similarly, the ellipticity χ, an angle that defines the amount of the elliptic nature from the circular shape, is

$$\tan(2\chi) = \frac{S_3}{\sqrt{S_1^2 + S_2^2}} = \frac{|a_l|^2 - |a_r|^2}{|a_l^* a_r|}. \quad (10)$$

After performing the straightforward calculations, one can easily express the Stokes parameters in terms of the longitudinal and transverse components of the second-order conductivity and incident polarization angle as $S_0 = |\sigma^{(2)}_L|^2 + |\sigma^{(2)}_T|^2$ and

$$S_1 = \left(|\sigma^{(2)}_L|^2 - |\sigma^{(2)}_T|^2 \right) \cos(2\phi) - 2|\sigma^{(2)}_L||\sigma^{(2)}_T| \cos \delta \sin(2\phi),$$

$$S_2 = 2\sqrt{S_0^2 - S_1^2} |\sigma^{(2)}_L||\sigma^{(2)}_T| \cos \delta_0,$$

$$S_3 = 2\sqrt{S_0^2 - S_1^2} |\sigma^{(2)}_L||\sigma^{(2)}_T| \sin \delta_0. \quad (11)$$

The phase difference between the longitudinal and transverse components is denoted by $\delta = \delta_L - \delta_T$. The cosine of the phase difference between a_x and a_y, i.e., $\delta_0 = \delta_y - \delta_x$, is obtained as (see the Appendix)

$$\cos \delta_0 = \frac{X}{\sqrt{X^2 + Y^2}}, \quad (12)$$

where we define $X = -(|\sigma^{(2)}_L|^2 - |\sigma^{(2)}_T|^2) \sin(2\phi) - 2|\sigma^{(2)}_L||\sigma^{(2)}_T| \cos \delta \cos(2\phi)$ and $Y = 2|\sigma^{(2)}_T||\sigma^{(2)}_L| \sin \delta$. In addition to these angular quantities, the state or character of the polarization is assigned by another dimensionless parameter, known as helicity (see the Appendix):

$$h = \frac{|a_l|^2 - |a_r|^2}{|a_l|^2 + |a_r|^2} = \frac{2\text{Im}[a_x a_y^*]}{|a_x|^2 + |a_y|^2} = \sin(2\chi). \quad (13)$$

Here the sign of the helicity decides the left- or right-handed character of the SHG signal. Specifically, if $h = +1$, the light is completely right-handed in nature, while $h = -1$ refers to the left-handed character of the light. Note that the helicity is proportional to the phase difference of the longitudinal and transverse response, $h \propto \sin \delta$, which can be utilized by probing the value of δ. The presented formalism for the computation of the nonlinear polarization quantities, Faraday rotation and ellipticity, is general and applicable for all systems. In this work, we discuss the case for the time-reversal symmetric and inversion symmetry broken system $1T'$-WTe$_2$.

III. RESULTS AND DISCUSSION

In this section, we present our numerical results and discuss the frequency and bias potential dependence of the nonlinear conductivity. Particularly, we report the polarization analysis by evaluating a nonvanishing Faraday rotation and the helicity of the SHG signal in single-layer $1T'$-WTe$_2$.

A. Frequency dependence of the second-order susceptibility

In Fig. 3, we plot three independent tensor elements of the nonlinear susceptibility as a function of the scaled incident frequency $\hbar\omega/\mu$. The absence of inversion symmetry leads to the spin-polarized band structure; however, the second-order response function is spin degenerate due to the time-reversal invariance. Although both one- and two-photon interband resonances are present, the two-photon resonance $\hbar\omega_\Sigma = 2\mu$ that occurs at $\hbar\omega/\mu = 1$ is less pronounced in $\chi^{(2)}_{yxx}$ owing to the absence of the corresponding two-photon vertex coupling $\kappa_{xy} = 0$. The situation does not remain the same in the case of $\chi^{(2)}_{xxy}$ and $\chi^{(2)}_{yyy}$, where both one-photon and two-photon absorption processes contribute to the diamagnetic and paramagnetic susceptibilities. Further, the shape of these interband resonances can be understood through the anisotropic Fermi surface in the k_x-k_y 2D momentum plane. The presence of the $v_y k_y$ term along the y component of the Pauli basis in the modeled Hamiltonian creates the anisotropy in the Fermi surface of WTe$_2$. On moving towards the higher momentum values, the quadratic term Bk^2 becomes large over the linear terms which ultimately suppress the anisotropic behavior of the Fermi surface and turn the surface into a more isotropic form at larger k. In addition to the two interband resonances, we find another peak for $\hbar\omega > 2\mu$ in Figs. 3(b) and 3(f). This arises due to the presence of the fundamental gap 2δ at the Γ point ($k = 0$), and for $\delta = 0$, the latter peak is absent. In addition to these features, we check the tunability of the second-order susceptibility by altering the bias potential U, and we observe strong dependence on U.

The spin-polarized dispersion has different band gaps at two valley points in the presence of a finite bias potential U.
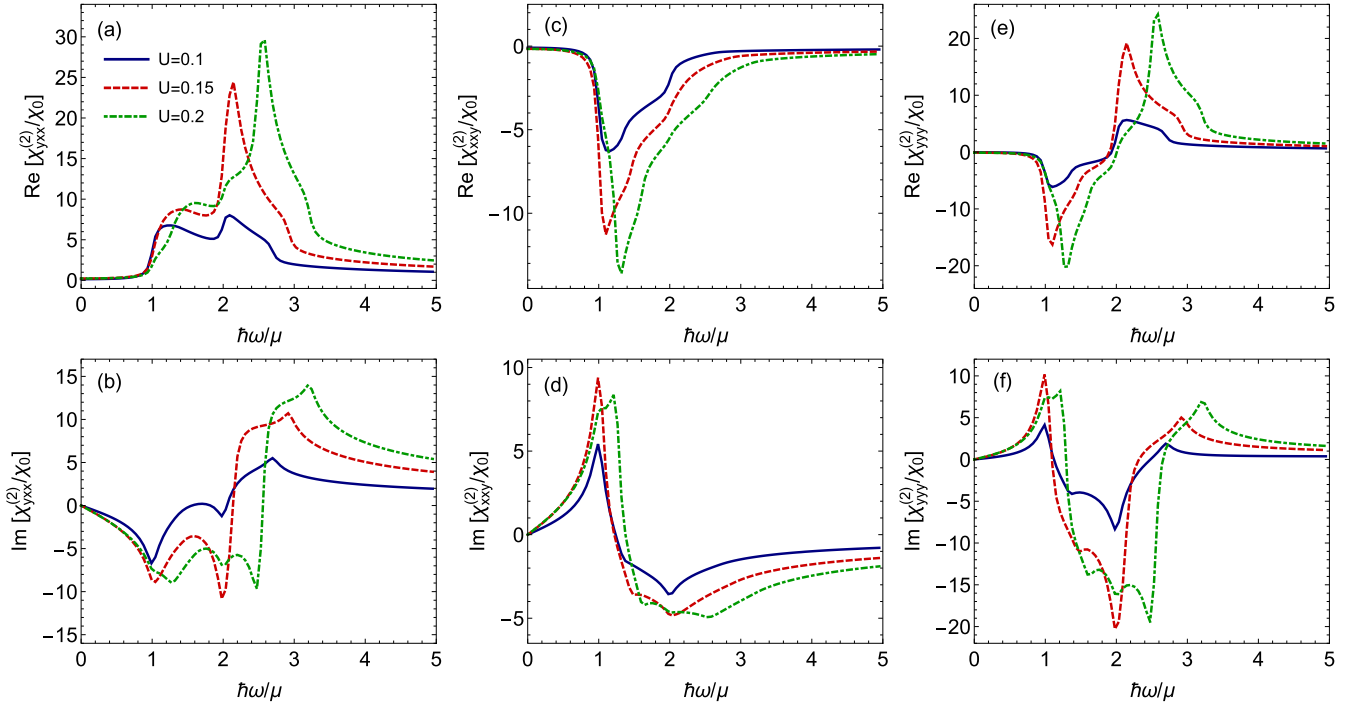
FIG. 3. The real and imaginary parts of three distinct components of the second-order susceptibility in response to the linearly polarized beam at three different bias potential values as a function of an incident energy scaled by the chemical potential. Here we set the parameters $A = 0$, $\delta = -0.25$ eV, $B = 1$ eV Å^2, $v_x = 0.1$ eV Å, $v_y = 0.3$ eV Å, $\mu = 0.2$ eV, and $\chi_0 = -e^3 v_y/(4\pi^2 \hbar^2)$.

For a large value of U and given the spin (e.g., spin up), which corresponds to green curves in Fig. 3, the chemical potential lies within the conduction band at valley $\mathbf{Q}' = -\mathbf{Q}$, while it is inside the band gap at valley $\mathbf{Q}$. Accordingly, the spin-conserved transitions at two-photon and one-photon transition edges at valley $\mathbf{Q}'$ follow $\hbar\omega = \mu$ and $\hbar\omega = 2\mu$, while in the other valley we have a two-photon peak at $\hbar\omega = \Delta_+$ with $\Delta_\pm = |U \pm v_x Q|$ and one-photon resonance $\hbar\omega = 2\Delta_+$. The two resonances at $\hbar\omega = 2\mu$ and $\hbar\omega = 2\Delta_+$ manifest as a double-peak profile. This double-peak structure is more visible in the imaginary part of the response function depicted in Figs. 3(b), 3(d), and 3(f). The real-part plots reveal a weak peak at $\hbar\omega = 2\mu$ for larger U.

B. Effect of bias potential

To track the evolution of the nonlinear response with the out-of-plane electric field, we plot the real and imaginary parts of the second-order susceptibility versus the bias potential U at the frequency $\hbar\omega = 2\mu$, where all responses contribute significantly, as seen in Fig. 3. We set the other parameters as $\mu = 0.1$ eV, $B = 1$ eV Å^2, $v_x = 0.1$ eV Å, $v_y = 0.3$ eV Å, and $\delta = -0.25$ eV for three elements, yxx, xxy, and yyy, in Fig. 4.

In the absence of the bias potential, $U = 0$, the second harmonic susceptibility vanishes owing to the preserved inversion symmetry. Thus, one requires a finite U to break the inversion symmetry which gives a nonzero response. By increasing U, the band gap around Q points widens and further enhances the susceptibility, as shown in Fig. 4. For small values of $U < \mu$ the response function linearly depends on the bias potential as the Fermi level lies within the conduction band. The response function changes sign when $U \to -U$, which implies that

it must be an odd function of U. For larger U that is still smaller than $\hbar\omega$, we notice some resonances due to interband transitions at $\hbar\omega = 2\mu + v_x Q$. The vanishing response for a higher amplitude of the bias potential U is because of the forbidden interband transitions for $\hbar\omega < \Delta_+$ due to the Pauli blocking. The presence of an external electric field can alter the bias potential and therefore control the value of second-order response in the distorted monolayer WTe$_2$.

C. Helicity and Faraday rotation of the second harmonic signal

Before we analyze the helicity of the SHG signal in $1T'$-WTe$_2$, it is useful to discuss it for trigonal prismatic TMD systems such as single-layer MoS$_2$. In single-layer MoS$_2$ the helicity vanishes due to the mirror ($x \to -x$) and threefold symmetries. Under mirror and threefold symmetries, the only nonzero tensor elements are given by $-\sigma_{yyy}^{(2)} = \sigma_{xxy}^{(2)} = \sigma_{xyx}^{(2)} = \sigma_{yxx}^{(2)}$. Accordingly, we have $(\sigma_L^{(2)}, \sigma_T^{(2)}) = -\sigma_{yyy}^{(2)}(\sin(3\phi), \cos(3\phi))$. Here the longitudinal and transverse conductivity components are in phase ($\delta = 0$), and therefore, the helicity vanishes, i.e., $h \propto \sin\delta = 0$. This result implies that not every noncentrosymmetric system can generate a second harmonic signal with a finite helicity. The finite helicity is the result of the chirality of the system, similar to the optical activity effects [92].

In Figs. 5(a) and 5(b), we plot the Faraday rotation angle ψ/π and helicity versus the incident energy $\hbar\omega$ at fixed $\delta = -0.25$ eV and $\mu = 0.1$ eV. In general, the Faraday rotation and helicity depend on the incident polarization angle ϕ. Here we consider the polarization angle $\phi = \pi/6$; thus, the value of $|\psi|$ for $\hbar\omega_\Sigma < 2\mu$ approaches an asymptotic finite value due to the presence of a nonlinear transverse current
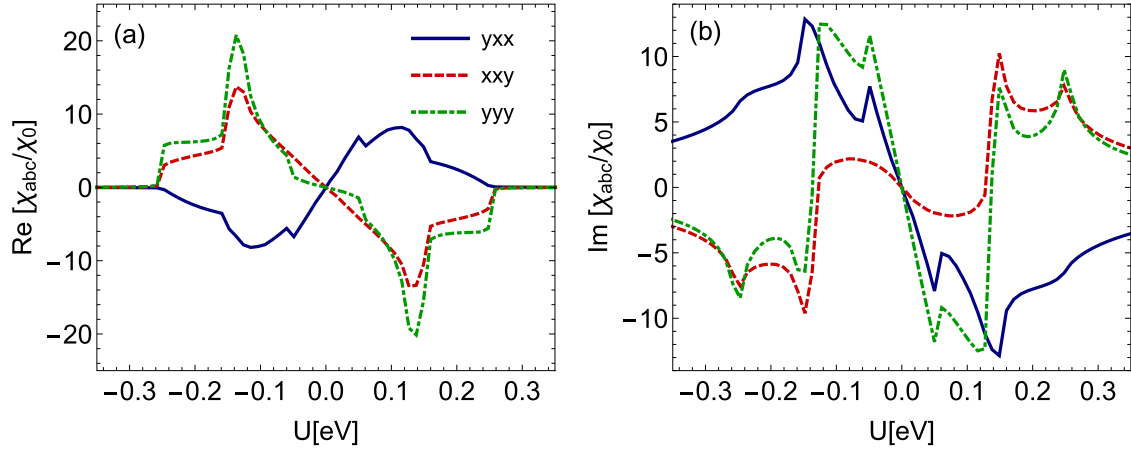
FIG. 4. Plot of the different components of the (a) real and (b) imaginary parts of the nonlinear susceptibility as a function of the bias potential at $\hbar\omega = 0.2$ eV. Here we set the parameters as $\mu = 0.1$ eV, $\delta = -0.25$ eV, $v_x = 0.1$ eVÅ, $v_y = 0.3$ eVÅ, and $B = 1$ eVÅ^2.

component. At low excitation energy $\hbar\omega_\Sigma \leqslant 2\mu$, the real part of the nonlinear response function goes to zero, which implies a vanishing helicity since $a_{x,y}$ are purely real valued.

At $\hbar\omega_\Sigma > 2\mu$, both the real and imaginary parts of the second-order response are finite, as shown Fig. 3, because the interband transitions lead to a nonvanishing helicity. This is a signature of the conversion of the linearly polarized light into the right-handed polarization with double frequency. As the energy approaches two times the value of the chemical potential, the system shows maximum positive helicity. At ex-
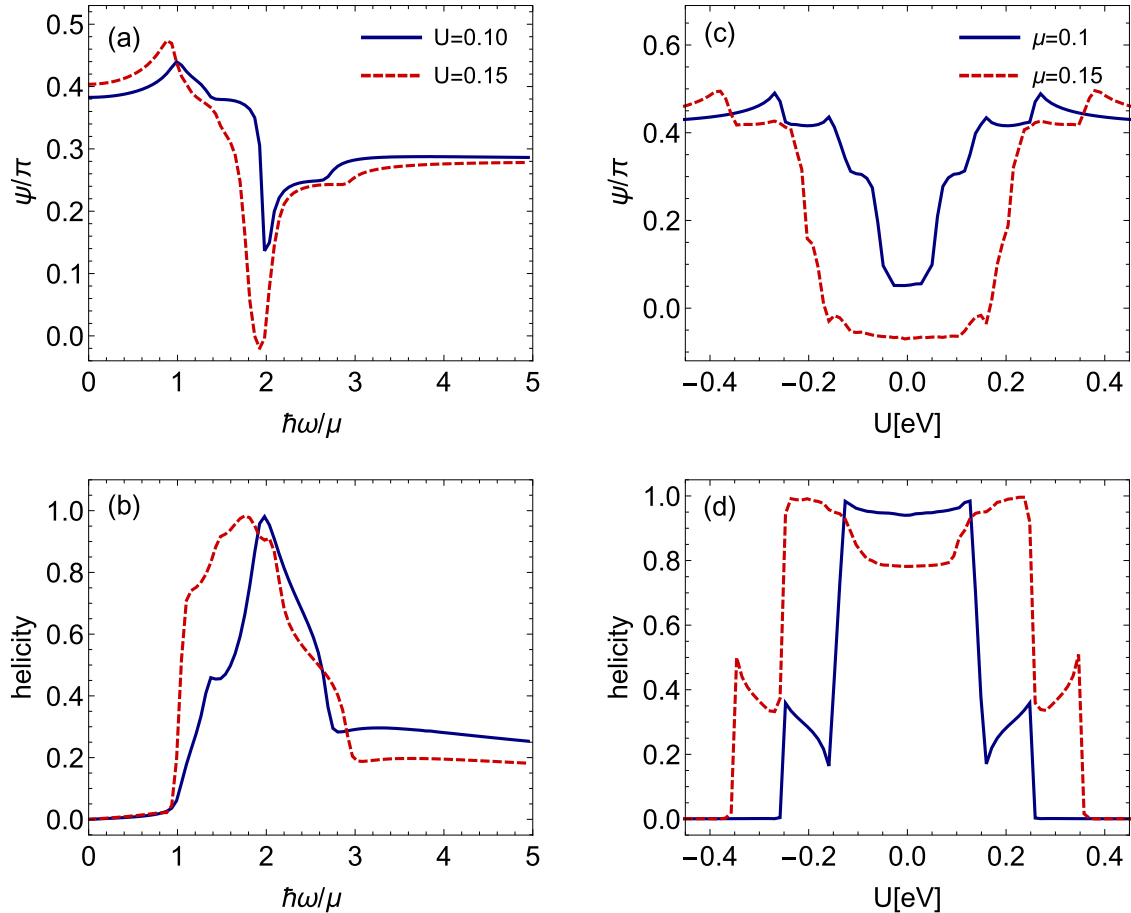

FIG. 5. (a) Faraday rotation angle and (b) helicity as a function of scaled incident energy at distinct values of U, but fixed $\mu = 0.1$ eV and $\delta = -0.25$ eV. (c) and (d) The same, but with the bias potential U at an incident energy twice the chemical potential for two different values of the chemical potential and fixed $\delta = -0.25$ eV, $B = 1$ eV Å^2, $v_x = 0.1$ eV Å, $v_y = 0.3$ eV Å, and polarization angle $\phi = \pi/6$.

treme higher energies, the second-order conductivity changes monotonically by $\hbar\omega$, which ultimately yields a saturation behavior in the Faraday angle and the helicity in the high-energy regime. In addition to the energy variation of the quantities, we also observe that the increase in the bias potential displaces the overall behavior of the polarization quantities towards the higher-energy values due to the significant variations in the band structure of $1T'$-WTe$_2$, as discussed earlier in the case of second-order response.

To elaborate on the bias potential effect, we show the results for the Faraday angle and helicity of $1T'$-WTe$_2$ at one-photon resonance frequency $\hbar\omega = 2\mu$ in Figs. 5(c) and 5(d), which corresponds to the maximum light conversion to the right-handed state of the polarization. For a given chemical potential and one-photon resonance condition for the frequency, we can notice a sudden jump from vanishing helicity to a finite value at $\Delta_- = U - v_x Q = 2\mu$ for $U > 0$. A further decrease of the bias potential by the vertical electric field leads to another jump to a larger value of the helicity at $\Delta_- = U - v_x Q = \mu$. For a wide range around small U the helicity is almost full, $h \sim 1$. The corresponding kinks are also visible in the Faraday rotation angle plot versus the bias potential. By moving the Fermi level within the conduction band to higher energy, the number of available states for conduction increases. This ultimately shifts the helicity jump locations to higher values $\mu + v_x Q$ and $2\mu + v_x Q$. Since the interband transitions are not allowed at $|U| > 2\mu$ for $\hbar\omega = 2\mu$, the helicity vanishes for large bias potential, as shown in Fig. 5(d). Furthermore, the behavior of the Faraday rotation angle and helicity remain symmetrical on interchanging the sign of the bias potential.

Finally, we refer to the experimental setup [26] for the dual-gated device of the encapsulated single-layer WTe$_2$ between thin layers of hexagonal boron nitride (hBN) that demonstrate the tuning potential of an external vertical electric field. The corresponding electrical gating results in the net displacement electrical field (or bias potential) between the top and bottom atomic layers which breaks the inversion symmetry. The bias potential is determined by the relation $U \approx e\epsilon E_z d$, where ϵ is the dielectric constant of hBN, E_z is the external vertical electric field, and d is the separation between the top and bottom atomic layers of $1T'$-WTe$_2$. By setting $E_z \approx 0.1 \text{V/nm}$, $\epsilon \approx 3$, and $d \approx 0.31$ nm [93,94], the above formula implies $U \sim 0.1$ eV, where we have theoretically observed the maximum susceptibility and the highest second harmonic helicity.

IV. SUMMARY

To summarize, we studied the Faraday rotation angle and helicity for the second harmonic radiation in an inversion symmetry broken, distorted, and gated 2D single-layer $1T'$-WTe$_2$. To compute the second harmonic helicity, we first calculate second-order conductivity within a diagrammatic framework. We found that the linearly polarized light shows maximum conversion into a second harmonic signal with right- or left-handed helicity on propagating through the system when the incident energy is in resonance with the interband transition edges. We identified that the linear-to-circular conversion is pronounced only within the window of the two-photon transition edge due to the encapsulated features of the band structure of the system. Our results pave the way for future helicity spectroscopy experiments which may help us to probe hidden topology in the nonlinear spectroscopy.

APPENDIX: DERIVATION OF THE FARADAY ROTATION ANGLE AND HELICITY

Consider a linearly polarized incident beam of light striking at the 2D material interface $z = 0$ in the xy plane which is defined as

$$\boldsymbol{E} = \hat{\boldsymbol{\epsilon}}(\phi) E_0 e^{i(\mathbf{q}\cdot\mathbf{r}-\omega t)} + \text{c.c.}, \tag{A1}$$

where the polarization unit vector is $\hat{\boldsymbol{\epsilon}}(\phi) = \hat{\mathbf{x}}\cos\phi + \hat{\mathbf{y}}\sin\phi$, $\mathbf{q}$ is the photon wave vector, ϕ is the polarization angle in the $\hat{x}$ direction, ω is the frequency of the incoming beam, E_0 is the amplitude of the beam, and t refers to time. By definition, the second harmonic current reads

$$J_a^{(2)}(2\omega) = \sigma_{abc}^{(2)}(2\omega; \omega, \omega) E_b(\omega) E_c(\omega). \tag{A2}$$

In terms of the longitudinal and transverse components, the second-order current can be decomposed as follows:

$$\mathbf{J}^{(2)} = J_L^{(2)} \hat{\boldsymbol{\epsilon}}(\phi) + J_T^{(2)} \hat{\mathbf{t}}(\phi). \tag{A3}$$

Note that the transverse unit vector $\hat{\mathbf{t}}(\phi) = \hat{\mathbf{z}} \times \hat{\boldsymbol{\epsilon}}(\phi) = \hat{\mathbf{y}}\cos\phi - \hat{\mathbf{x}}\sin\phi$. We define the nonlinear conductivity associated with the longitudinal and transverse directions:

$$\sigma_L^{(2)} = J_L^{(2)}/\mathcal{E}_0^2 = a_x\cos\phi + a_y\sin\phi, \quad \sigma_T^{(2)} = J_T^{(2)}/\mathcal{E}_0^2 = -a_x\sin\phi + a_y\cos\phi. \tag{A4}$$

Here the coefficients a_x and a_y can be calculated by writing $a_x = |a_x|e^{i\delta_x}$ and $a_y = |a_y|e^{i\delta_y}$. From Eq. (A4), we have

$$a_x = \sigma_L^{(2)}\cos\phi - \sigma_T^{(2)}\sin\phi = |\sigma_L^{(2)}|e^{i\delta_L}\cos\phi - |\sigma_T^{(2)}|e^{i\delta_T}\sin\phi, \tag{A5}$$

$$a_y = \sigma_L^{(2)}\sin\phi + \sigma_T^{(2)}\cos\phi = |\sigma_L^{(2)}|e^{i\delta_L}\sin\phi + |\sigma_T^{(2)}|e^{i\delta_T}\cos\phi. \tag{A6}$$

Straightforward algebraic calculation yields the norm of a_x and a_y as

$$|a_x| = \sqrt{|\sigma_L^{(2)}|^2\cos^2\phi + |\sigma_T^{(2)}|^2\sin^2\phi - |\sigma_L^{(2)}||\sigma_T^{(2)}|\cos(\delta)\sin(2\phi)}, \tag{A7}$$

$$|a_y| = \sqrt{\left|\sigma_{\mathrm{L}}^{(2)}\right|^2 \sin^2\phi + |\sigma_{\mathrm{T}}^{(2)}|^2 \cos^2\phi + |\sigma_{\mathrm{L}}^{(2)}||\sigma_{\mathrm{T}}^{(2)}|\cos(\delta)\sin(2\phi)}. \tag{A8}$$

Similarly, the phase difference is given by

$$\tan(\delta_0) = \frac{2\left|\sigma_{\mathrm{T}}^{(2)}\right|\left|\sigma_{\mathrm{L}}^{(2)}\right|\sin(\delta)}{2\left|\sigma_{\mathrm{T}}^{(2)}\right|\left|\sigma_{\mathrm{L}}^{(2)}\right|\cos(\delta)\cos 2\phi + \left(\left|\sigma_{\mathrm{T}}^{(2)}\right|^2 - \left|\sigma_{\mathrm{L}}^{(2)}\right|^2\right)\sin 2\phi}, \tag{A9}$$

where $\delta_0 = \delta_y - \delta_x$ and $\delta = \delta_{\mathrm{L}} - \delta_{\mathrm{T}}$. Stokes parameters for the monochromatic light consist of four scalar values related to the polarization angles [89–91],

$$
\begin{aligned}
S_0 &= |a_x|^2 + |a_y|^2, \\
S_1 &= |a_x|^2 - |a_y|^2 = S_0 \cos(2\chi)\cos(2\psi), \\
S_2 &= 2|a_x||a_y|\cos\delta_0 = S_0 \cos(2\chi)\sin(2\psi), \\
S_3 &= 2|a_x||a_y|\sin\delta_0 = S_0 \sin(2\chi).
\end{aligned}
\tag{A10}
$$

Here S_0 represents the irradiance of the light beam, S_1 denotes the dominant character of the horizontal and vertical components based on the sign, S_2 refers to the orientation of the ellipse, S_3 corresponds to the handedness of the polarization state, ψ is the angle of rotation made by polarized light with respect to the x axis or the original semimajor axis, and χ is the ellipticity, which defines the angular amount of ellipse from the circular shape. Similarly, in the circular basis $(\hat{l}, \hat{r})$ we can define the following parameters:

$$
\begin{aligned}
S_0 &= |a_l|^2 + |a_r|^2, \quad S_1 = 2\mathrm{Re}(a_l^* a_r), \\
S_2 &= -2\mathrm{Im}(a_l^* a_r), \quad S_3 = |a_l|^2 - |a_r|^2.
\end{aligned}
\tag{A11}
$$

Now, on dividing S_2 by S_1, the Faraday rotation angle can be obtained as

$$\tan(2\psi) = \frac{S_2}{S_1} = \frac{2|a_x||a_y|\cos\delta_0}{|a_x|^2 - |a_y|^2}. \tag{A12}$$

Similarly, the ellipticity can be calculated using the relation

$$\tan(2\chi) = \frac{S_3}{\sqrt{S_1^2 + S_2^2}} = \tan\delta_0 \sin(2\psi). \tag{A13}$$

The helicity, which is the ratio of the handedness of the polarization state and the irradiance of the light beam, is defined as

$$h = \frac{|a_l|^2 - |a_r|^2}{|a_l|^2 + |a_r|^2} = \frac{S_3}{S_0}. \tag{A14}$$

Using the relation for the ellipticity, the helicity becomes

$$h = \sin(2\chi). \tag{A15}$$

[1] J. Heising and M. G. Kanatzidis, J. Am. Chem. Soc. **121**, 638 (1999).

[2] G. Eda, T. Fujita, H. Yamaguchi, D. Voiry, M. Chen, and M. Chhowalla, ACS Nano **6**, 7311 (2012).

[3] X. Qian, J. Liu, L. Fu, and J. Li, Science **346**, 1344 (2014).

[4] K. F. Mak, K. He, J. Shan, and T. F. Heinz, Nat. Nanotechnol. **7**, 494 (2012).

[5] K.-A. N. Duerloo, M. T. Ong, and E. J. Reed, J. Phys. Chem. Lett. **3**, 2871 (2012).

[6] S. N. Shirodkar and U. V. Waghmare, Phys. Rev. Lett. **112**, 157601 (2014).

[7] J. Jiang, F. Tang, X. C. Pan, H. M. Liu, X. H. Niu, Y. X. Wang, D. F. Xu, H. F. Yang, B. P. Xie, F. Q. Song, P. Dudin, T. K. Kim, M. Hoesch, P. K. Das, I. Vobornik, X. G. Wan, and D. L. Feng, Phys. Rev. Lett. **115**, 166601 (2015).

[8] E. Bruyer, D. Di Sante, P. Barone, A. Stroppa, M.-H. Whangbo, and S. Picozzi, Phys. Rev. B **94**, 195402 (2016).

[9] Z. Z. Du, H.-P. Wang, C. M. Sun, H.-Z. Lu, and X. C. Xie, Nat. Commun. **12**, 5038 (2021).

[10] A. N. Morozovska, E. A. Eliseev, G. I. Dovbeshko, M. D. Glinchuk, Y. Kim, and S. V. Kalinin, Phys. Rev. B **102**, 075417 (2020).

[11] S. Guddala, F. Komissarenko, S. Kiriushechkina, A. Vakulenko, K. Chen, A. Alu, V. M. Menon, and A. B. Khanikaev, Nat. Commun. **12**, 3746 (2021).

[12] A. R. Khan, L. Zhang, K. Ishfaq, A. Ikram, T. Yildrim, B. Liu, S. Rahman, and Y. Lu, Adv. Funct. Mater. **32**, 2105259 (2022).

[13] Y. Shao et al., Proc. Natl. Acad. Sci. USA **118**, e2116366118 (2021).

[14] Z. Z. Du, H.-Z. Lu, and X. C. Xie, Nat. Rev. Phys. **3**, 744 (2021).

[15] Q. Ma, A. G. Grushin, and K. S. Burch, Nat. Mater. **20**, 1601 (2021).

[16] S. Tang et al., Nat. Phys. **13**, 683 (2017).

[17] J. H. Garcia, M. Vila, C.-H. Hsu, X. Waintal, V. M. Pereira, and S. Roche, Phys. Rev. Lett. **125**, 256603 (2020).

[18] Z. Fei, W. Zhao, T. A. Palomaki, B. Sun, M. K. Miller, Z. Zhao, J. Yan, X. Xu, and D. H. Cobden, Nature (London) **560**, 336 (2018).

[19] C. Huang et al., ACS Nano **12**, 7185 (2018).

[20] P. Sharma, F.-X. Xiang, D.-F. Shao, D. Zhang, E. Y. Tsymbal, A. R. Hamilton, and J. Seidel, Sci. Adv. **5**, eaax5080 (2019).

[21] H. Yang, S. W. Kim, M. Chhowalla, and Y. H. Lee, Nat. Phys. **13**, 931 (2017).

[22] Z. Li, Y. Song, and S. Tang, J. Phys.: Condens. Matter **32**, 333001 (2020).

[23] Z.-Y. Jia, Y.-H. Song, X.-B. Li, K. Ran, P. Lu, H.-J. Zheng, X.-Y. Zhu, Z.-Q. Shi, J. Sun, J. Wen, D. Xing, and S.-C. Li, Phys. Rev. B **96**, 041108(R) (2017).

[24] S. Nandy and D. A. Pesin, SciPost Phys. **12**, 120 (2022).

[25] Z. Fei, T. Palomaki, S. Wu, W. Zhao, X. Cai, B. Sun, P. Nguyen, J. Finney, X. Xu, and D. H. Cobden, Nat. Phys. **13**, 677 (2017).

[26] S.-Y. Xu, Q. Ma, H. Shen, V. Fatemi, S. Wu, T.-R. Chang, G. Chang, A. M. M. Valdivia, C.-K. Chan, Q. D. Gibson, J. Zhou, Z. Liu, K. Watanabe, T. Taniguchi, H. Lin, R. J. Cava, L. Fu, N. Gedik, and P. Jarillo-Herrero, Nat. Phys. **14**, 900 (2018).

[27] H. Min, B. Sahu, S. K. Banerjee, and A. H. MacDonald, Phys. Rev. B **75**, 155115 (2007).

[28] J. B. Oostinga, H. B. Heersche, X. Liu, A. F. Morpurgo, and L. M. K. Vandersypen, Nat. Mater. **7**, 151 (2008).

[29] Y. Zhang, T.-T. Tang, C. Girit, Z. Hao, M. C. Martin, A. Zettl, M. F. Crommie, Y. R. Shen, and F. Wang, Nature (London) **459**, 820 (2009).

[30] T. Taychatanapat and P. Jarillo-Herrero, Phys. Rev. Lett. **105**, 166601 (2010).

[31] L. Muechler, A. Alexandradinata, T. Neupert, and R. Car, Phys. Rev. X **6**, 041069 (2016).

[32] L.-K. Shi and J. C. W. Song, Phys. Rev. B **99**, 035403 (2019).

[33] A. Lau, R. Ray, D. Varjas, and A. R. Akhmerov, Phys. Rev. Materials **3**, 054206 (2019).

[34] K.-A. N. Duerloo, Y. Li, and E. J. Reed, Nat. Commun. **5**, 4214 (2014).

[35] D.-H. Choe, H.-J. Sung, and K. J. Chang, Phys. Rev. B **93**, 125109 (2016).

[36] M. M. Ugeda, A. Pulkin, S. Tang, H. Ryu, Q. Wu, Y. Zhang, D. Wong, Z. Pedramrazi, A. Martín-Recio, Y. Chen, F. Wang, Z.-X. Shen, S.-K. Mo, O. V. Yazyev, and M. F. Crommie, Nat. Commun. **9**, 3401 (2018).

[37] W. Zhao, E. Runburg, Z. Fei, J. Mutch, P. Malinowski, B. Sun, X. Huang, D. Pesin, Y.-T. Cui, X. Xu, J.-H. Chu, and D. H. Cobden, Phys. Rev. X **11**, 041034 (2021).

[38] Q. H. Wang, K. Kalantar-Zadeh, A. Kis, J. N. Coleman, and M. S. Strano, Nat. Nanotechnol. **7**, 699 (2012).

[39] T. Mueller and E. Malic, npj 2D Mater. Appl. **2**, 29 (2018).

[40] G. Soavi, G. Wang, H. Rostami, D. G. Purdie, D. De Fazio, T. Ma, B. Luo, J. Wang, A. K. Ott, D. Yoon, S. A. Bourelle, J. E. Muench, I. Goykhman, S. Dal Conte, M. Celebrano, A. Tomadin, M. Polini, G. Cerullo, and A. C. Ferrari, Nat. Nanotechnol. **13**, 583 (2018).

[41] P. Bhalla, M.-X. Deng, R.-Q. Wang, L. Wang, and D. Culcer, Phys. Rev. Lett. **127**, 206801 (2021).

[42] Y. Wang, F. Iyikanat, H. Rostami, X. Bai, X. Hu, S. Das, Y. Dai, L. Du, Y. Zhang, S. Li, H. Lipsanen, F. J. García de Abajo, and Z. Sun, Adv. Mater. **34**, 2107104 (2022).

[43] S. Klimmer, O. Ghaebi, Z. Gan, A. George, A. Turchanin, G. Cerullo, and G. Soavi, Nat. Photonics **15**, 837 (2021).

[44] I. Sodemann and L. Fu, Phys. Rev. Lett. **115**, 216806 (2015).

[45] Y. Zhang, Y. Sun, and B. Yan, Phys. Rev. B **97**, 041101(R) (2018).

[46] J.-S. You, S. Fang, S.-Y. Xu, E. Kaxiras, and T. Low, Phys. Rev. B **98**, 121109(R) (2018).

[47] J. Quereda, T. S. Ghiasi, J.-S. You, J. van den Brink, B. J. van Wees, and C. H. van der Wal, Nat. Commun. **9**, 3346 (2018).

[48] J. I. Facio, D. Efremov, K. Koepernik, J.-S. You, I. Sodemann, and J. van den Brink, Phys. Rev. Lett. **121**, 246403 (2018).

[49] A. Fleischer, O. Kfir, T. Diskin, P. Sidorenko, and O. Cohen, Nat. Photonics **8**, 543 (2014).

[50] F. de Juan, A. G. Grushin, T. Morimoto, and J. E. Moore, Nat. Commun. **8**, 15995 (2017).

[51] Q. Ma, S.-Y. Xu, C.-K. Chan, C.-L. Zhang, G. Chang, Y. Lin, W. Xie, T. Palacios, H. Lin, S. Jia, P. A. Lee, P. Jarillo-Herrero, and N. Gedik, Nat. Phys. **13**, 842 (2017).

[52] E. C. I. van der Wurff and H. T. C. Stoof, Phys. Rev. B **96**, 121116(R) (2017).

[53] M. Sabbaghi, H.-W. Lee, and T. Stauber, Phys. Rev. B **98**, 075424 (2018).

[54] H. Rostami and M. Polini, Phys. Rev. B **97**, 195151 (2018).

[55] F. de Juan, Y. Zhang, T. Morimoto, Y. Sun, J. E. Moore, and A. G. Grushin, Phys. Rev. Research **2**, 012017(R) (2020).

[56] J. H. Cullen, P. Bhalla, E. Marcellina, A. R. Hamilton, and D. Culcer, Phys. Rev. Lett. **126**, 256601 (2021).

[57] O. Matsyshyn and I. Sodemann, Phys. Rev. Lett. **123**, 246602 (2019).

[58] K. Kang, T. Li, E. Sohn, J. Shan, and K. F. Mak, Nat. Mater. **18**, 324 (2019).

[59] Y. Shi, J. Kahn, B. Niu, Z. Fei, B. Sun, X. Cai, B. A. Francisco, D. Wu, Z.-X. Shen, X. Xu, D. H. Cobden, and Y.-T. Cui, Sci. Adv. **5**, eaat8799 (2019).

[60] P. Bhalla, A. H. MacDonald, and D. Culcer, Phys. Rev. Lett. **124**, 087402 (2020).

[61] P. Bhalla, Phys. Rev. B **103**, 115304 (2021).

[62] L. Mennel, M. M. Furchi, S. Wachter, M. Paur, D. K. Polyushkin, and T. Mueller, Nat. Commun. **9**, 516 (2018).

[63] J. E. Moore and J. Orenstein, Phys. Rev. Lett. **105**, 026805 (2010).

[64] P. Hosur, Phys. Rev. B **83**, 035309 (2011).

[65] Q. Ma *et al.*, Nature (London) **565**, 337 (2019).

[66] Z. Z. Du, C. M. Wang, H.-Z. Lu, and X. C. Xie, Phys. Rev. Lett. **121**, 266601 (2018).

[67] P. Bhalla, K. Das, D. Culcer, and A. Agarwal, arXiv:2108.04082

[68] X. Zhang, L. Li, X. Zhu, X. Liu, Q. Zhang, P. Lan, and P. Lu, Phys. Rev. A **94**, 053408 (2016).

[69] X. Zhang, J. Li, Z. Zhou, S. Yue, H. Du, L. Fu, and H.-G. Luo, Phys. Rev. B **99**, 014304 (2019).

[70] A. Chacón, D. Kim, W. Zhu, S. P. Kelly, A. Dauphin, E. Pisanty, A. S. Maxwell, A. Picón, M. F. Ciappina, D. E. Kim, C. Ticknor, A. Saxena, and M. Lewenstein, Phys. Rev. B **102**, 134115 (2020).

[71] R. E. F. Silva, A. Jimenez-Galan, B. Amorim, O. Smirnova, and M. Ivanov, Nat. Photonics **13**, 849 (2019).

[72] M. Faraday, Philos. Trans. R. Soc. London **136**, 1 (1846).

[73] E. A. Stern, J. C. McGroddy, and W. E. Harte, Phys. Rev. **135**, A1306 (1964).

[74] R. F. O'Connell and G. Wallace, Phys. Rev. B **26**, 2231 (1982).

[75] R. W. Boyd, *Nonlinear Optics* (Academic, London, 2008).

[76] D. Budker, W. Gawlik, D. F. Kimball, S. M. Rochester, V. V. Yashchuk, and A. Weis, Rev. Mod. Phys. **74**, 1153 (2002).

[77] P. R. Berman, Am. J. Phys. **78**, 270 (2010).

[78] N. Bloembergen, *Nonlinear Optics* (World Scientific, Singapore, 1996).

[79] A. Sarsen and C. Valagiannopoulos, Phys. Rev. B **99**, 115304 (2019).

[80] C. A. Valagiannopoulos, M. Mattheakis, S. N. Shirodkar, and E. Kaxiras, J. Phys. Commun. **1**, 045003 (2017).

[81] M. Papaj and L. Fu, Phys. Rev. Lett. **123**, 216802 (2019).

[82] C. L. Kane and E. J. Mele, Phys. Rev. Lett. **95**, 226801 (2005).

[83] H. Rostami, M. I. Katsnelson, G. Vignale, and M. Polini, Ann. Phys. (NY) **431**, 168523 (2021).

[84] A. Säynätjoki, L. Karvonen, H. Rostami, A. Autere, S. Mehravar, A. Lombardo, R. A. Norwood, T. Hasan, N. Peyghambarian, H. Lipsanen, K. Kieu, A. C. Ferrari, M. Polini, and Z. Sun, Nat. Commun. **8**, 893 (2017).

[85] G. D. Mahan, *Many-Particle Physics* (Springer, Berlin, 2013).

[86] D. E. Parker, T. Morimoto, J. Orenstein, and J. E. Moore, Phys. Rev. B **99**, 045121 (2019).

[87] H. Rostami and V. Juričić, Phys. Rev. Research **2**, 013069 (2020).

[88] H. Rostami, arXiv:2204.08060.

[89] W. H. McMaster, Am. J. Phys. **22**, 351 (1954).

[90] J. D. Jackson, *Classical Electrodynamics*, 3rd ed. (Wiley, New York, 1999).

[91] P. E. Artal, *Handbook of Visual Optics* (CRC Press, Boca Raton, FL, 2017).

[92] L. D. Barron, *Molecular Light Scattering and Optical Activity* (Cambridge University Press, Cambridge, 2009).

[93] Akash Laturia, M. L. Van de Put, and W. G. Vandenberghe, npj 2D Materials and Applications **2**, 6 (2018).

[94] V. Shahnazaryan, O. Kyriienko, and H. Rostami, Phys. Rev. B **100**, 165303 (2019).